Shock Waves (2006) 15:241–246
DOI 10.1007/s00193-006-0023-4

ORIGINAL ARTICLE

Navier–Stokes computations in micro shock tubes

David E. Zeitoun · Yves Burtschell

Received: 29 September 2005 / Accepted: 1 February 2006 / Published online: 14 June 2006

Abstract Micro shock tube flows were simulated using unsteady 2D Navier–Stokes equations combined with boundary slip velocities and temperature jumps conditions. These simulations were performed using the parallel version of a multi-block finite-volume home code. Different initial low pressures and shock tube diameters allow to have the scaling ratio $ReD/4L$ vary. The numerical results show a strong attenuation of the shock wave strength with a decrease of the hot flow values along the tube. When the scaling ratio decreases the shock waves can transform into compression waves. Comparison to the existing 1D models also shows the limit of these models.

Keywords Micro shock tube · Navier–Stokes equations · Slip conditions · Finite-volume method

PACS 47.15 Gf · 47.45 Gx · 52.35 Tc

1 Introduction

In the past, the flow-field in a shock tube has been widely studied from theoretical, experimental and numerical points of view (see Glass and Sislian [1]). The hot flow parameters are well described by the Hugoniot's relations in the most classical shock tubes. It is also well known that for a given diameter D of the tube, when the initial pressure P_1 of the driven gas decreases, the unsteady wall boundary layer development in the hot gas may strongly modify the behavior of this flow [2]. In particular, one can notice a decrease of shock wave strength M_s and an increase of the contact velocity to a limiting regime where the shock and contact surface move at the same velocity and the distance between them tends to a constant value L_m. In the hot flow the parameters are not constant, due to the boundary layer interaction with the hot flow. It was shown that this distance L_m is proportional to P_1D^2 and the quantity $L_\mathrm{m}/(DRe_1)$ with $Re_1 = \varrho aD/\mu$, tends to a constant value when M_s increases [3,4]. A detailed comparison between experiments and numerics in the case of 5 cm shock tube diameter and low initial driven gas pressure can be found in Zeitoun and Imbert [5]. It is important to notice that in all these studies, the shock tube flow is split in an inviscid core flow and a wall boundary layer.

In the last decade, due to the development and design of certain microelectromechanical systems (MEMS), a lot of studies were published for a better understanding of the gas dynamic flows in these microscale geometries. But few works concern shock wave propagations or high-speed flows [6,7] in these microscales where the Reynolds number is low and where the viscous and heat effects play an important role compared to the convection ones. Recently, shock wave propagation with initial $M_\mathrm{s} = 1.2$ in 2D narrow channels with height ranging from 1 to 16 mm was performed numerically and experimentally [8]. In this paper, the authors claimed that 'viscous effects in channel become noticeable for height lower than 4 mm, even at atmospheric pressure'. In the same way, Brouillette [9] studied the flow-field in a micro shock tube with 5.3 mm diameter and different driver/driven pressure ratios. He showed, through

---

Communicated by K. Takayama.

D. E. Zeitoun (✉) · Y. Burtschell
Université de Provence, Polytech'Marseille, Dpt ME,
IUSTI/UMR CNRS 6595 Technopôle de Château Gombert,
5 rue Enrico Fermi, 13013 Marseille, France
e-mail: David.Zeitoun@polytech.univ-mrs.fr

pressure measurements, that the effects are stronger than those given through his 1D modeling and the coupling between the size and the initial pressure can be characterized by the following scaling ratio ($Re_1 D/4L$). The lower this quantity is, the stronger the effects are. But as pointed out by Brouillette [9], the choice of the L value (distance between the shock and the contact surface) in this scaling ratio is problematic because it is not known and can be very short for a low-pressure shock tube.

In these microflows, it is well known that the Reynolds number is connected to the Knudsen number $Kn = \lambda/D$ (λ is the mean free path of the molecule) by the following relation $Kn \simeq M/Re$ and the unsteady Navier–Stokes equations modeling these flows are valid only if $Kn \prec 0.01$ with no-slip boundary conditions and can be extended to $Kn \simeq 0.1$ with slip boundary conditions [10].

This paper describes the application of the unsteady axisymmetric Navier–Stokes equations with the classical or velocity slip and temperature jump boundary conditions to these micro shock tube flows. H_2/N_2 are the driver/driven gas and the ratio between the length and the diameter of the driven tube is $L/D = 100$. This ratio is usual in the classical shock tube. The first case considered is to study these unsteady flows with two diaphragm pressure ratios corresponding to theoretical Mach numbers equal, respectively, to 5 and 3. The second case is focused on $Ms_{\mathrm{th}} = 3$ with a decrease of initial pressure where the slip boundary conditions are included in the computations and where the initial pressure and diameter are modified by keeping the same value of $P_1 D^2$.

2 Governing equations and numerical description

Compressible laminar unsteady viscous flows are governed by the Navier–Stokes equations coupled with the multi-species conservation equations for a mixture. This set of equations may be written in a compact integral conservative form as

$$\int_V \frac{\partial U}{\partial t}\,\mathrm{d}V + \int_S F\,\mathrm{d}S - \int_S G\,\mathrm{d}S = 0,$$

where the volume of a computational cell is denoted by V and its surface by S and

$$U = [\rho_i, \rho\mathbf{V}, E]^{\mathrm{T}},$$
$$F = [\rho_i(\mathbf{V}\cdot\mathbf{n}), \rho\mathbf{V}(\mathbf{V}\cdot\mathbf{n}) + p\mathbf{n}, (E+p)(\mathbf{V}\cdot\mathbf{n})]^{\mathrm{T}},$$
$$G = [\rho_i\mathbf{V}_i^{\mathrm{d}}, \boldsymbol{\tau}^{\mathrm{s}}, \boldsymbol{\tau}^{\mathrm{s}}\cdot\mathbf{V} + \mathbf{q}^{\mathrm{s}}\cdot\mathbf{n}]^{\mathrm{T}},$$
$$\boldsymbol{\tau}^{\mathrm{s}} = \bar{\bar{\tau}}\cdot\mathbf{n}.$$

Quantities ρ_i, p,$\mathbf{V} = [u, v]^{\mathrm{T}}$ and E are, respectively, the density of the ith species, the pressure, the velocity vector and the total energy per unit volume; $\mathbf{V}_i^{\mathrm{d}}$ being the diffusion velocity of the ith species and

$$E = \rho\left(e + \frac{\mathbf{V}^2}{2}\right),$$

where e is the internal energy per unit mass defined by

$$e = \sum_{i=1}^{N} Y_i e_i(T).$$

$Y_i = \rho_i/\rho$ is the mass fraction of each species, ρ_i is the density of each species, the subscript $i = 1, 2$ represents the species involved in the driver/driven mixture, ρ is the density of the mixture and

$$e_i(T) = \frac{3}{2}R_i T + \psi_i(e_{\mathrm{rot},i}(T)).$$

$\psi_i = 0$ for atoms or 1 for molecules. p is the pressure of the mixture determined from the Dalton law $p = \sum_i p_i$, where p_i is the partial pressure of the ith species, assumed to behave as a perfect gas following the relation $P_i = \rho_i(R/M_i)T$, where M_i is the mass per mole of the ith species. $\rho_i = \rho Y_i$ being the mass of ith species, per unit volume and R denotes the universal perfect gas constant. $\bar{\bar{\tau}}$ and $\mathbf{q}^{\mathrm{s}}$ are, respectively, the viscous stress tensor and the heat flux vector.

The computations of these equations were performed by using the parallel version of a multi-block finite-volume home code (named CARBUR, Burtschell et al. [11]) with an exact Riemann solver coupled with AUSM-DV solver and second-order MUSCL extrapolation for the inviscid fluxes. The viscous and heat transfer terms were discretized using a central difference scheme. Grid cells were refined near the wall and the mesh size is (400×60) in x, y directions with a minimum non-dimensional y/D step equal to 1×10^{-2} at the wall which leads to an integration time step of 10^{-9} s when the initial low pressure is 100 Pa.

2.1 Boundary conditions for continuum approach

On the solid walls the following boundary conditions were used:

$$u = v = 0, \quad T = T_{\mathrm{w}}, \quad \frac{\partial p}{\partial n} = 0,$$

where the subscript w refers to the wall quantities.

To take into account the effects of rarefaction when the initial low pressure decreases, the slip velocity and temperature jump boundary conditions for the continuum approaches were used. Different expressions of these boundary conditions can be found in the literature, but most of them have the same structure and differ not significantly in values of the numerical coefficients.

In the present paper, the following slip velocity and temperature jump boundary conditions are employed [12]:

$$u_{\mathrm{s}} - u_{\mathrm{w}} = \frac{1.012}{\rho}\sqrt{\frac{2}{RT}}\mu\left(\frac{\partial u_\tau}{\partial n}\right)_{\mathrm{w}},$$

$$T_{\mathrm{s}} - T_{\mathrm{w}} = 1.173\frac{\gamma}{\gamma-1}\frac{1}{Pr}\frac{\sqrt{\pi}}{\rho\sqrt{8RT}}\mu\left(\frac{\partial T}{\partial n}\right)_{\mathrm{w}}.$$

Here the subscript s refers to the gas quantities near the wall; u_τ is the tangential velocity, Pr the Prandtl number and γ the ratio of specific heats.

3 Numerical results and discussion

The initial conditions of the different test cases are given in Table 1. The initial temperatures of the driven and driver gases are equal to 300 K and is the same for all cases. The scaling ratio $Re_1D/4L$ varies between 0.25 and 0.025. The shock tube diameter and the length of the driven tube are, respectively, 5 mm and 50 cm. The subscript '1' refers to the driven tube conditions.

Figure 1 represents the evolution of the shock wave location along the tube for two first test cases which correspond to theoretical Mach numbers Ms_{th}, respectively, equal to 5 and 3. In this figure the diaphragm is located at the origin of the x axis. Due to the considered tube length, the second case $Ms_{\mathrm{th}} = 3$ leads to a stronger attenuation of the Mach number and its value is about 1.02 after a distance of 42 cm along the tube. This unsteady evolution shows that to calculate an experimental Mach number in this tube, the two pressure transducers have to be close. For this case, the temperature and pressure profiles along the tube axis are plotted for different times in Fig. 2. The strong attenuation is also clearly visible. At the last computational time $t = 7.8310^{-4}$ s, the maximum of temperature behind the shock wave is 337 K and does not correspond to the value given by Hugoniot's relation with the local Mach number. It can also be noticed that the pressure increases continuously, which can be seen from the pressure profile, without a plateau behind the shock wave. This was pointed out experimentally by Brouillette [9]. For this time, Fig. 3 shows the temperature iso-contours in the tube. The zone of higher temperature is confined to the central part of the tube and this indicates that the viscous and dissipation effects play an important role. It is also clear that the flow cannot be split into an inviscid part and a wall boundary layer and that all approaches based on this assumption do not work.

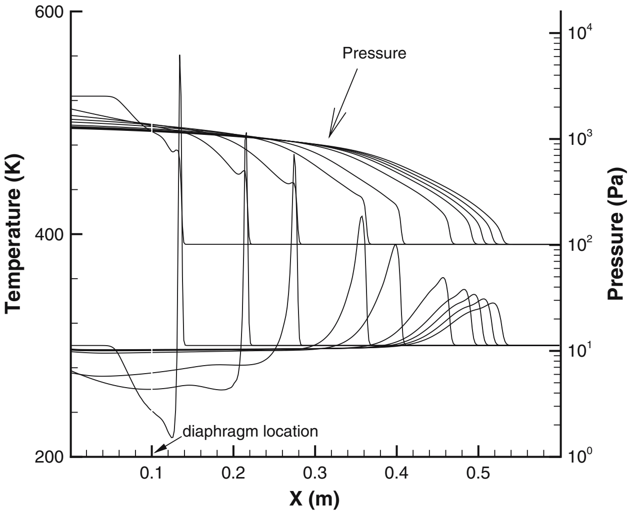

Fig. 2 Temperature profiles along the shock tube at different times for case 2

For studying the effect of the scaling ratio $Re_1D/4L$ on the shock wave propagation, this ratio is red uced by a factor of 10 through the initial pressure ($P_1 = 10$ Pa) (see case 3 in Table 1.) and is equal to 0.025.

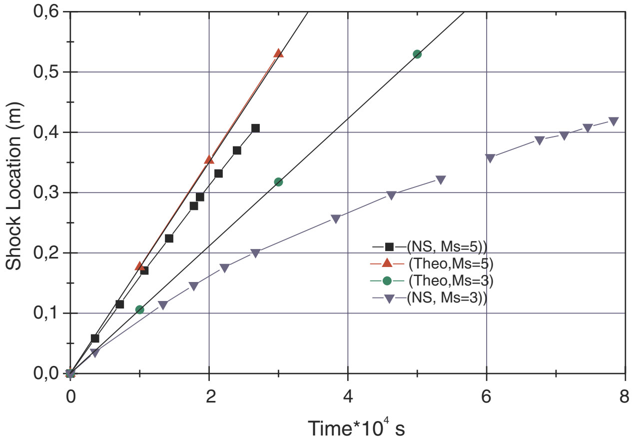

Fig. 1 Shock wave location versus time for the cases 1 and 2

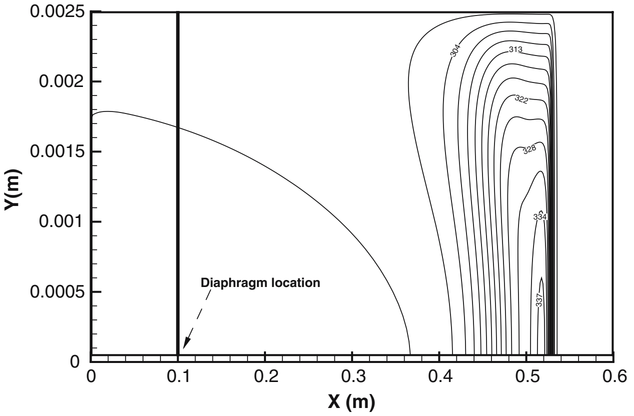

Fig. 3 Temperature iso-contours at $t = 7.8310^{-4}$ s for the test case 2

Table 1 Initial conditions of the test case computations

Case	Ms_{th}	P_4/P_1	P_1 (Pa)	$Re_1 D/4L$
1	5	156	100	0.25
2	3	25.04	100	0.25
3	3	25.04	10	0.025
4	3[a]	25.04	10	0.025
5	3[a]	25.04	40	0.1

[a] With slip boundary conditions

The unsteady computations are conducted with the classical or velocity slip and temperature jump boundary conditions. In this case, the computational time step is also reduced by a factor of 10. The shock Mach number evolutions along the tube are plotted in Fig. 4 for the same initial pressure ratio with the classical or velocity slip and temperature jump boundary conditions in the computations. These curves confirm that the shock wave attenuation is a function of pressure for the same tube diameter. The more the initial pressure decreases the stronger this attenuation is. This is due to the boundary layer thickness which is inversely proportional to the low pressure chamber and the mass and energy losses in the core flow increase when this thickness increases. The shock wave vanishes and transforms into compression waves and the Mach number tends to a constant value equal to 0.54. Moreover, the slip boundary conditions reduce this effect slightly as shown in Fig. 5 where the isotherms are plotted at the same time after the diaphragm opening. This indicates that the slip boundary conditions reduce the viscous effects and lead to a core flow which is more pronounced behind the shock wave with a higher temperature value and a distance behind the shock and the contact surface more clearly visible.

Another case (case 5 in Table 1) with the scaling ratio $Re_1 D/4L$ equal to 0.1 has been computed and the shock location evolution along the tube is compared to the other cases in Fig. 6. This evolution is about the same as the previous case with $Re_1 D/4L = 0.025$ and tends to the same slope value of 0.54 at the end of the computational time. This result seems to predict a limiting regime of wave propagation when the scaling ratio decreases.

Now, a shock tube with 50 μm diameter is used and the initial pressure is taken equal to 10^5 Pa in order to keep constant the scaling ratio $Re_1 D/4L = 0.025$ with the same value $L = 0.5$ m. It is obvious that this value of L is too long. It is the reason why the computational domain is limited to a value equal to 0.05 m. The cell number is the same as before and the slip boundary conditions are also included in the present computations. The evolution of the shock wave location is plotted in Fig. 7 with the results of test cases 3 and 4 given in Table 1. The shape of this evolution along the tube is nearly the same but the values are slightly lower than in

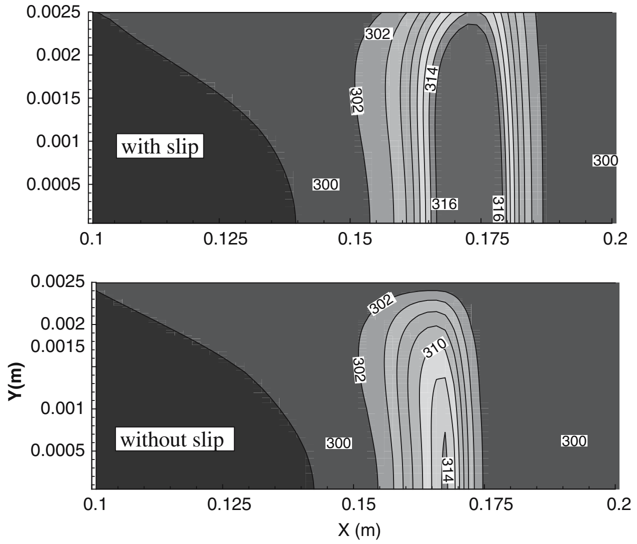

Fig. 5 Temperature iso-contours at $t = 1.810^{-4}$ s for the without and with slip condition: cases 3 and 4

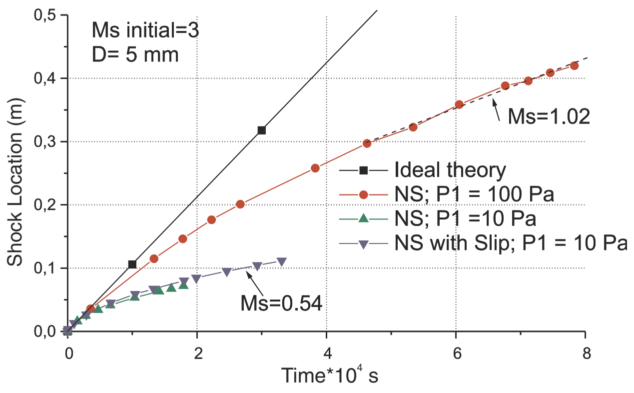

Fig. 4 Shock wave location versus time for the two different initial low pressures: cases 2 and 3

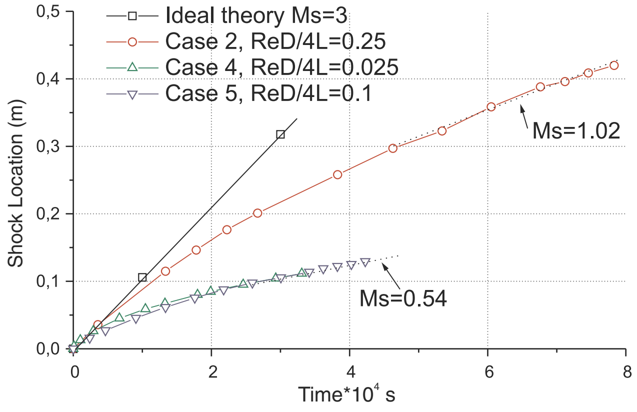

Fig. 6 Shock wave location versus time for $Ms_{\text{th}} = 3$ and different low initial pressure

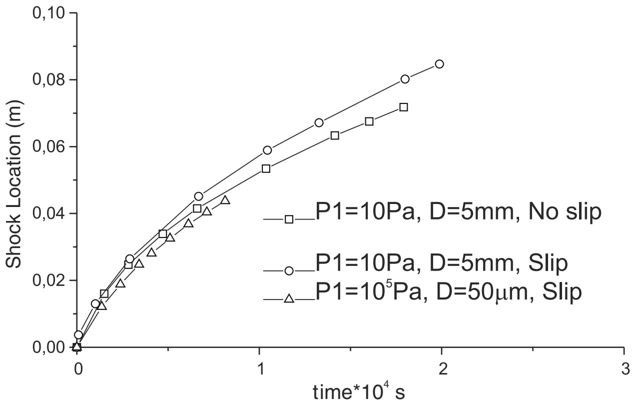

Fig. 7 Shock wave location versus time for $Ms_{\text{th}} = 3$

the previous case 4. It is to note that these two cases have the same value of P_1D^2. Figure 8 presents a comparison of the isotherms between the fourth case of Table 1 and this last case. The shock wave appears thinner and the effect of the slip boundary conditions are less pronounced in this last case. This is mainly due to the initial pressure of the driven gas which modifies the Reynolds number Re_1 and a value of $L = 0.05$ m which leads to $Re_1D/4L = 0.25$, more appropriate in regard to the results plotted in Fig. 3.

4 Comparison with previous models

In an ideal shock tube, the fixed initial conditions in high and low pressure chambers allow to calculate the final state properties and wave speeds of the shock tube flow. As an example the diaphragm pressure ratio P_4/P_1 required for a given Mach number M_s is obtained as

$$\left[\frac{P_4}{P_1}\right]_{\text{ideal}} = \left[1+\frac{2\gamma_1}{\gamma_1+1}\left(M_s^2-1\right)\right],$$

$$\left[1-\frac{\gamma_4-1}{\gamma_4+1}\left(\frac{a_1}{a_4}\right)\left(M_s-\frac{1}{M_s}\right)\right]^{-2\gamma_4/(\gamma_4-1)},$$

where a is the speed of sound. But it is well known that when the low pressure in the driven tube or/and its diameter decreases, the real-gas effects play an important role through the interaction between the boundary layer development and the core flow. This effect was experimentally observed by Duff [2] who proposed the following expression in order to take into account:

$$\left[\frac{P_4}{P_1}\right]_{\text{Duff}} = \left[\frac{P_4}{P_1}\right]_{\text{ideal}},$$

$$\left(1+\frac{M_s^2+\beta_1-1}{(\beta_1-1)[M_s^2(\beta_1+1)-1]}\right)^{(\beta_1+1)/2},$$

where $\beta_1 \equiv (\gamma+1)/(\gamma-1)$.

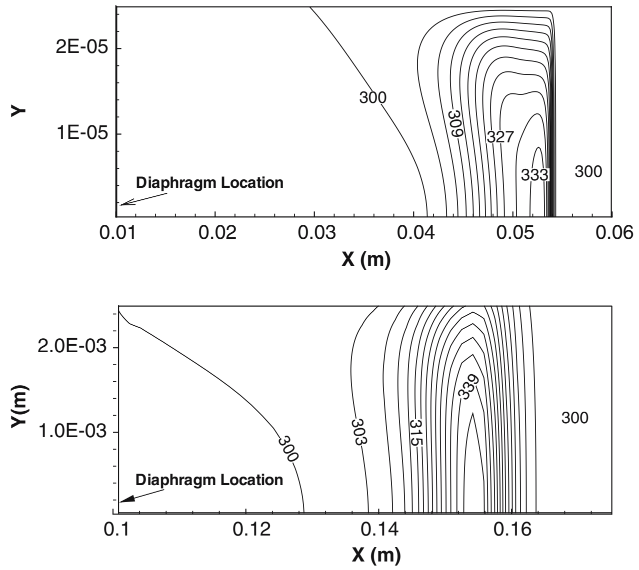

Fig. 8 Temperature iso-contours at $t = 0.8510^{-4}$ s (*upper* = $P_1 = 10^5$ Pa, $D = 50\,\mu$m, *lower*=$P_1 = 10$ Pa, $D = 5$ mm)

This effect also leads to an unsteady evolution of the flow parameters to a steady state, where the shock wave and the contact surface move with the same velocity. Unsteady computations with boundary layer/core flow coupling were made for describing this evolution along the shock tube [5]. From these computations a modified value of $\beta = 2.2$ seems more adapted and will be used in the previous expression. It is to note that this modified value is not connected to γ. More recently, from combining the conservation relations including viscous and heat transfer effects in 1D model, Brouillette [9] proposed two equations. One is the Raleigh line equation given by

$$\frac{P_2}{P_1} = 1+\gamma_1\left[M_s^2+\frac{4L}{DRe}M_s\right]\left(1-\frac{\rho_1}{\rho_2}\right).$$

The second one is the implicit equation for the Hugoniot curve which can be expressed as

$$\frac{P_2}{P_1} = \frac{\rho_2}{\rho_1}\left\{1+\frac{\gamma_1-1}{2}M_s^2\left[1+\left(\frac{\rho_1}{\rho_2}\right)^2\right] - \left(\frac{4L}{DRe}\right)\frac{1}{M_sPr}\left[\frac{P_2}{P_1}\frac{\rho_1}{\rho_2}-1\right]\right\}.$$

The intersection of the Raleigh line with Hugoniot's curve can be computed to obtain the 'jump conditions' for a given value of the scaling ratio $ReD/4L$. These conditions have to be connected to the diaphragm pressure ratio by an unsteady expansion. In Fig. 9 the diaphragm pressure ratio is plotted for different Mach numbers and the value of $ReD/4L$ given by Brouillette's model. The curves given the modified Duff's model and the ideal theory are also reported. It can be pointed out that the

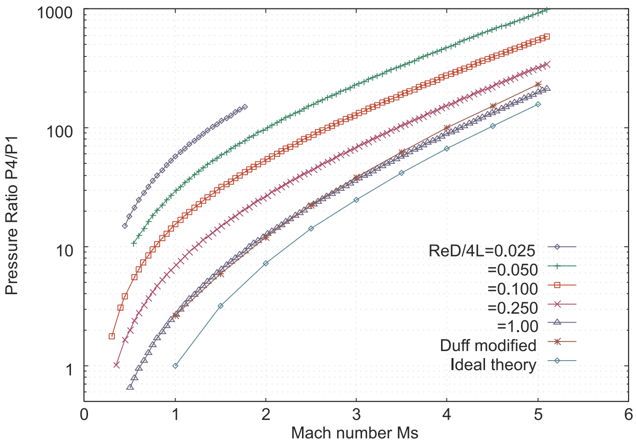

Fig. 9 Diaphragm pressure ratio versus Mach number from different theories ($\gamma_1 = 1.4$)

curve given by Brouillette's model with $ReD/4L = 1$ is identical to the one given by the modified Duff's model. It can also be deduced that the following relation $M_\mathrm{s} = M_\mathrm{s}^\mathrm{ideal}(1 - 1/\beta_1)$ given by Mirels [4] describes approximately the discrepancy between the ideal theory and Duff's relation. These curves also show that to obtain a given Mach number in a shock tube the diaphragm pressure ratio should strongly increase when $ReD/4L$ decreases. As an example with $ReD/4L = 0.05$, the diaphragm pressure ratio has to be one order higher to obtain a Mach number $M_\mathrm{s} = 2$ in the shock tube.

Now for a given diaphragm pressure ratio or ideal Mach number $M_\mathrm{s}^\mathrm{ideal}$, it is possible to plot the Mach number function of $ReD/4L$ as shown in Fig. 10 for $M_\mathrm{s}^\mathrm{ideal} = 3$. In this figure, the Mach number obtained by the present computations is also plotted for the different test cases. The numerical results show that the shock wave attenuation is stronger than those given by previous theories. This is due to the important unsteady 2D behavior of the flow along the tube with a strong interaction between the boundary layer and the hot flow.

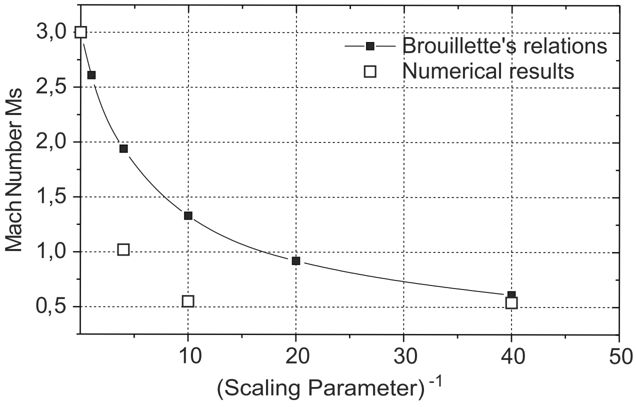

Fig. 10 Mach number function of the scaling ratio $ReD/4L$ for a $M_\mathrm{s}^\mathrm{ideal} = 3$

5 Conclusion

The creation and the propagation of a shock wave in micro shock tube has been investigated numerically for different initial pressure ratios and diameters. The attenuation of the shock wave intensity is stronger for lower initial pressure or/and for smaller tube diameter. These shock waves can be transformed to compression waves along the tube. The flow-field behind the shock wave cannot be split in to inviscid/viscous part as used in the previous models. The slip boundary conditions become important for the computational results at low values of the scaling. In order to compare different shock tube flows through the scaling ratio $Re_1D/4L$, the choice of L has to be specified. Finally, it is not easy to produce experimental results in the micro shock tube but they will be useful to validate the analytical or numerical description of these flows.

References

1. Glass, I.I., Sislian, J.P.: Nonstationary flows and shock waves. Oxford Sciences Publications, Oxford (1994)
2. Duff, R.E.: Shock tube performance at initial low pressure. Phys. Fluids **4**(2), 207 (1959)
3. Roshko, A.: On flow duration in low pressure shock tube. Phys. Fluids **3**(9), 807 (1960)
4. Mirels, H.: Test time in low pressure shock tubes. Phys. Fluids **6**(9), 1201 (1963)
5. Zeitoun, D.E., Imbert, M.: Interaction between the unsteady boundary layer and Inviscid hot flow in a shock tube. AIAA J. **17**(8), 821 (1979)
6. Oh, C.K., Oran, E.S., Sinkovits, R.S.: Computations of high speed, high Knudsen number microchanels flows. J. Thermophys. Heat Transf. **11**(4), 497 (1997)
7. Raju, R., Roy, S.: Hydrodynamic prediction of high speed microflows, AIAA paper 4010. In: 33rd AIAA Fluid Dynamics Conference, 23–26 June, Orlando, FL, USA (2003)
8. Sun, M., Ogawa, T., Takayama, K.: Shock propagation in narrow channels. In: Lu, F.K. (ed.) Proceedings of 24th International Sympesium on Shock Waves, p. 1321 (2001)
9. Brouillette, M.: Shock waves at microscales. Shock Wave J. **13**, 3–12 (2003)
10. Karniadakis, G.E.M., Beskok, A.: Micro Flows fundamentals and Simulation. Springer, Berlin Heidelberg New York (2000)
11. Burtschell, Y., Cardoso, M., Zeitoun, D.E.: Numerical analysis of reducing driver gas contamination in impulse shock tunnels. AIAA J. **39**(12), 2357–2365 (2001)
12. Kogan, M.N.: Rarified Gas Dynamics. Plenum Press, New York (1969)